Remote imprinting of moiré lattices

Jie Gu[1,2*], Jiacheng Zhu[1*], Patrick Knuppel[1], Kenji Watanabe[3], Takashi Taniguchi[3], Jie Shan[1,4,5**], Kin Fai Mak[1,4,5**]

[1]School of Applied and Engineering Physics, Cornell University, Ithaca, NY, USA
[2]State Key Laboratory of Surface Physics, Department of Physics, Fudan University, Shanghai, China
[3]National Institute for Materials Science, 1-1 Namiki, 305-0044 Tsukuba, Japan
[4]Laboratory of Atomic and Solid State Physics, Cornell University, Ithaca, NY, USA
[5]Kavli Institute at Cornell for Nanoscale Science, Ithaca, NY, USA

[*]These authors contributed equally: Jie Gu, Jiacheng Zhu
[**]Email: jie.shan@cornell.edu; kinfai.mak@cornell.edu

Two-dimensional (2D) moiré materials have emerged as an exciting platform for discoveries of new physics and device concepts [1-6]. These materials are formed by overlaying two layered crystals with small differences in orientation or/and lattice constant, the direct coupling of which generates moiré potentials. The moiré materials (such as doping density) are highly tunable, but the moiré lattices, once formed, cannot be easily altered. Here we demonstrate electrostatic imprinting of moiré lattices onto a monolayer semiconductor. The moiré potential is created by a lattice of electrons that is supported by a Mott insulator state in a remote $MoSe_2/WS_2$ moiré layer. The imprinted moiré potential generates flat bands and correlated insulating states in the target material, which are detected by an exciton sensor. It can be turned on/off by a gate voltage that controls the doping density only in the moiré layer. We also illustrate the interplay between the electrostatic and structural relaxation effects for moiré imprinting as a function of the target and moiré layer spacing. Our results demonstrate a pathway towards the gate control of moiré lattices in an arbitrary 2D semiconductor or semimetal.

In moiré materials with two directly coupled layers, moiré potentials are generated by periodic modulations with the moiré periodicity in interlayer tunneling, dielectric screening, and/or structural relaxations [1-11]. In the latter, the structural relaxation produces a periodic strain pattern and a smooth superlattice potential due to the strongly strain-dependent electronic band structure [10]. Although the moiré materials are highly tunable in the electronic doping density, bandwidth, and band topology [1-3, 5, 6], dynamical control of the moiré lattice (e.g. turning it on/off and/or modifying its symmetry) has remained challenging. A promising approach to overcome this limitation is to remotely imprint a moiré lattice onto a 2D target layer by the periodic electrostatic potential defined by the electron lattice in a semiconductor moiré layer [12]. Here the moiré and target layers are spatially separated by an insulating spacer with thickness thin compared to the moiré period (a_M). Both the depth and the symmetry of the superlattice potential can in principle be controlled by electrostatic gating (e.g., by setting the moiré layer to an

incompressible electron crystal state or a compressible fluid state), thereby allowing the dynamic control of the superlattice in the target layer.

To demonstrate this concept, we fabricate the vertical heterostructure shown in Fig. 1a (Extended Data Fig. 1). It consists of an angle-aligned $MoSe_2/WS_2$ moiré layer and a target $MoSe_2$ monolayer with large electron band mass. The two layers are not angle-aligned with each other so that interlayer tunneling is strongly suppressed [13]. The two layers are separated by a 4-layer thick hBN spacer in device 1 and a 2-layer hBN in device 2. The moiré layer has $a_M \approx 8$ nm due to the 4% lattice mismatch between $MoSe_2$ and WS_2 (Ref. [14]). The combined heterostructure is encapsulated between hBN and few-layer graphite top and bottom gates. The two gates allow independent tuning of the total electron doping density (ν, in units of the lattice filling factor) and the vertical electric field (E); the latter controls the electron distribution between the moiré and the target layer ($\nu = \nu_m + \nu_t$). Here ν_m and ν_t denote the electron doping density in the moiré and the target layer, respectively.

In order to probe the dielectric response of the combined (moiré plus target layer) system, we further insert a WSe_2 monolayer as an exciton sensor into the device [15]. The sensor is separated from the target layer by another 3-4-layer hBN spacer; it is kept charge neutral (Extended Data Fig. 2) and is non-perturbative to the physics of the target layer [15]. The 2s Rydberg state of the sensor is sensitive to the compressibility of the combined system; in particular, a blueshift and a spectral weight enhancement in the 2s Rydberg state signify the emergence of an incompressible state (Methods). Unless otherwise specified, all results are acquired at 5 K for electron doping ($\nu > 0$). See Methods for details on device fabrication and optical measurements.

Figure 1b shows the schematic electrostatics phase diagram (in ν and E) of the combined system. Similar phase diagram has also been observed in other 2D heterostructures with weak interlayer hopping [e.g., bilayer WSe_2 (Ref. [16-18]), AB-stacked $MoTe_2/WSe_2$ (Ref. [19, 20]) and Coulomb coupled WSe_2/WS_2 and WSe_2 (Ref. [21, 22]) etc.]. The grey-shaded area corresponds to sharing of electrons between the moiré and target layers. The black and pink solid line (determined based on the optical spectroscopy results in Extended Data Fig. 4 and 6) denotes the boundary for full charge transfer to the moiré and the target layer, respectively. The boundaries disperse in the phase diagram as ν and E changes the Fermi level and the relative band edge alignment of the combined system, respectively [20-22]. While the pink line displays no jumps in E as the Fermi level moves through the conduction band of the target layer, the jump at $\nu = 1$ and $\nu = 2$ for the black line corresponds to the finite Mott and moiré band gap in the moiré layer, respectively [20-22]. Moreover, the darker grey area bound by the pink dashed (dotted) lines corresponds to a fixed filling $\nu_m = 1$ ($\nu_m = 2$) in the moiré layer; here the Fermi level is inside the Mott or moiré band gap of the moiré layer as the doping density in the target layer varies [20]. See Methods for additional discussions on the electrostatics phase diagram.

Figure 1c-f correlates the reflectance contrast spectrum near the fundamental exciton resonances of the combined system (left panel) and that from the 2s Rydberg state of the sensor (right panel) for four representative cases of device 1 with: (c) $\nu_m = \nu_t = 0$, (d)

$\nu_m > 0$ and $\nu_t = 0$, (e) $\nu_m = 0$ and $\nu_t > 0$, and (f) $\nu_m > 0$ and $\nu_t > 0$. (We have taken an energy derivative of the 2s exciton reflectance contrast in order to enhance its visibility.) The dots in Fig. 1b with the same color as the spectrum locate the positions of the four cases in the electrostatics phase diagram. The corresponding band alignment for each case is also shown.

We can see that for (c) the fundamental exciton resonance of the moiré layer (MX_1) [23-25], the neutral exciton resonance of the target layer (X) and the sensor 2s resonance are all strong, as expected for all charge-neutral layers. In contrast, all of the exciton resonances turn weak in (f); here the neutral exciton features evolve into weaker charged exciton features [26] and the sensor 2s exciton is effectively screened by the compressible sample [15]. Finally, MX_1 turns weak and X remains strong for (d) while the reverse happens for (e). The 2s exciton is effectively screened in both cases but it shows a stronger redshift for (e) because of the closer proximity of the sensor to the target layer and therefore more effective screening [17, 27].

With the sensitivity of the various exciton resonances on doping and interlayer charge distribution established, we now focus on the sensor 2s exciton, which is sensitive to the compressibility of the sample [15] (see Extended Data Fig. 3 and 4 for a summary on other exciton resonances for device 1). Figure 2 shows the dependence of the 2s reflectance contrast spectrum on the total filling factor ν for three cases: $\nu_m > 0$ and $\nu_t = 0$ (Fig. 2a); $\nu_m = 0$ and $\nu_t > 0$ (Fig. 2b); and $\nu_m = 1$ and $\nu_t > 0$ (Fig. 2c). The three cases correspond to the arrowed trajectories in the phase diagram in Fig. 1b.

In Fig. 2a, the enhanced 2s reflectance contrast signals the emergence of correlated insulating states at $\nu = 1/3$, 1/2, 2/3 and 1 in the moiré layer. The fractional and the integer states are the charge-ordered states [14, 15, 28] and the Mott insulator [14, 28, 29], respectively. The results are fully consistent with doping only the moiré layer [14, 15, 28, 29].

Figure 2b shows the case of doping only the target layer. A sudden redshift in the 2s exciton (by ~ 25 meV) accompanied by a substantial reduction in its spectral weight is observed for $\nu > 0$. The result is consistent with the emergence of a compressible target layer upon electron doping. The redshift is substantially stronger than that for the compressible regions in the moiré layer in Fig. 2a because the target layer is spatially closer to the exciton sensor and therefore the 2s exciton is screened much more effectively by doping in the target layer [17, 27, 30].

Figure 2c shows the case of doping the target layer while keeping the moiré layer at the Mott insulating state at $\nu_m = 1$. Interestingly, compared to the case in Fig. 2b, we observe a new incompressible state at $\nu_t = 1$ (corresponding to $\nu = 2$) signaled by a blueshift in the 2s exciton. We summarize the results as a phase diagram in Fig. 4a, which plots the gate- and electric field-dependence of the 2s exciton resonance (see Methods for details of the analysis). An enhanced 2s exciton resonance signals the emergence of an incompressible state. The phase boundaries are also labeled similar to Fig. 1b. The new incompressible state appears only at $\nu_m = \nu_t = 1$.

Next we examine device 2, which has a thinner (2-layer thick) hBN spacer, under the same doping conditions as device 1 in Fig. 3. Compared to device 1, the main difference is that an incompressible state is also observed in the target layer at $\nu_t = 1$ even for $\nu_m = 0$. Figure 4b summarizes the phase diagram of device 2 by the 2s exciton reflectance contrast amplitude (see Extended Data Fig. 5 and 6 for other exciton resonances). In contrast to device 1, a $\nu_t = 1$ incompressible state is observed in the target layer irrespective of the doping in the moiré layer even when the latter is compressible (i.e., $0 < \nu_m < 1$ and $1 < \nu_m < 2$). Also, because of the robust incompressible state at $\nu_t = 1$ for any values of ν_m, there is now an electric field jump at $\nu = 1$ for the pink solid boundary; the jump is directly proportional to the $\nu_t = 1$ charge gap of the target layer [20, 21]. Moreover, there are now areas bound by the black dashed lines that correspond to fixed $\nu_t = 1$; here the Fermi level is inside the $\nu_t = 1$ charge gap of the target layer as ν_m varies.

We begin our discussions on device 1 (Fig. 2 and 4a). The observation of a new incompressible state at $\nu_m = \nu_t = 1$ demonstrates the presence of a moiré potential in the target layer when the moiré layer is doped at $\nu_m = 1$. The induced moiré potential cannot come from the negligible interlayer tunneling between the angle-misaligned moiré and target layers with a 4-layer thick hBN spacer [31]; the sensitivity of the $\nu_t = 1$ insulating state to ν_m is also inconsistent with the interlayer tunneling origin. The lattice relaxation contribution to the moiré potential is also unimportant because otherwise an incompressible state at $\nu_t = 1$ and $\nu_m = 0$ similar to that in device 2 would have emerged (see discussions below). In fact, the emergence of the incompressible state only at $\nu_m = \nu_t = 1$ is consistent with the remote imprinting of a moiré lattice onto the target layer by the periodic electrostatic potential of the Mott insulator in the moiré layer. In particular, electrons in the Mott insulator are organized into a triangular lattice by the strong on-site Coulomb repulsion in the moiré layer [32]. The triangular charge lattice is expected to imprint an electrostatic potential of honeycomb symmetry onto the target layer (Fig. 1a and Extended Data Fig. 7). The imprinted potential induces flat bands that substantially enhance the electronic correlations in the target layer, resulting in the correlated insulating state at $\nu_t = 1$.

In this picture, the new correlated insulating state is expected to disappear as the triangular charge lattice melts when the moiré layer is doped away from the Mott insulator [33] (consistent with Fig. 4a). The lack of correlated insulating states in the target layer at fixed $\nu_m = 1/3$, 1/2 and 2/3 can be explained by free carrier screening of the long-range Coulomb repulsions in the moiré layer by the target layer; the screening melts the charge-ordered states at fractional ν_m in the moiré layer [21] and the associated imprinted lattice. In other words, the combined (moiré plus target layer) structure should be treated as a single, correlated system for fractional ν_m (Ref. [34]). This is in contrast to the robust $\nu_m = 1$ Mott insulating state stabilized by the on-site Coulomb repulsion, in which free carrier screening is much less effective [7].

What is the nature of the $\nu_t = 1$ correlated insulating state? The state corresponds to a half-filled honeycomb lattice, which means that the translational symmetry of the imprinted lattice is spontaneously broken. Possible scenario include a triangular lattice

charge density wave, which spontaneously breaks the sublattice symmetry of the honeycomb lattice [35], and stripe phases, which spontaneously break both the translational and rotational symmetries [36]. We are not able to distinguish these possibilities at this point. Note that we also do not observe an insulating state at $\nu_t = 2$ and $\nu_m = 1$ likely because the imprinted moiré potential is not strong enough to stabilize a honeycomb lattice Mott insulator (see Methods for additional discussions).

Next, we discuss the results of device 2 (Fig. 3 and 4b). The observation of a $\nu_t = 1$ incompressible state in the target layer irrespective of ν_m demonstrates an imprinted moiré lattice beyond the electrostatics mechanism. The lack of an obvious electric field dependence for the $\nu_t = 1$ incompressible state at $\nu_m = 0$ also shows that the interlayer tunneling mechanism is irrelevant (resonance interlayer tunneling is expected to show strong electric field dependence near band inversion [14]). The most plausible origin for the moiré potential is thus from lattice relaxations in the structure [10], which produce a periodic strain pattern in the target layer. Such strain-induced moiré potential is known to be the dominant contribution in some semiconductor moiré bilayers [10]. Compared to the thicker hBN spacer in device 1, the thinner hBN spacer in device 2 favors a more substantial lattice relaxation, which in turn induces a strong enough moiré potential that can stabilize the $\nu_t = 1$ correlated insulating state irrespective of ν_m. This picture is further supported by Ref. [37], which reports an exponential decay of a moiré-induced lattice relaxation with the vertical distance from an embedded moiré layer.

Finally, we note that in addition to the strain contribution in device 2 there is also an electrostatics contribution to the moiré potential. The latter is signified by the monotonic increase in the 2s exciton reflectance contrast amplitude with increasing ν_m from $\nu_m = 0$ to 1 (Fig. 4b and Extended Data Fig. 8). The enhanced 2s amplitude reflects a larger charge gap for the $\nu_t = 1$ insulating state in the target layer [15]. As the density in the moiré layer increases from $\nu_m = 0$ to 1, the electrostatics contribution gains importance relative to the strain contribution, which is largely independent of ν_m. This in turn strengthens the total moiré potential and the $\nu_t = 1$ insulating state. However, it remains unclear at this point if the moiré potentials from the two contributions have the same symmetry and/or phase [38]. It would be interesting to explore in future studies the interplay of the two contributions with respect to their relative strengths, symmetries and phases.

In conclusion, we have demonstrated in this study remote imprinting of moiré lattice onto a monolayer semiconductor through a proximal semiconductor moiré bilayer. We have identified two separate contributions to the moiré potential: an electrostatically imprinted contribution and a lattice relaxation contribution; the dependence of their relative importance on the hBN spacer thickness has also been examined; the results have been reproduced in additional devices (Extended Data Fig. 9). Our study is distinct from Ref. [11] in both the origin of the imprinted moiré potential (periodic dielectric screening in Ref. [11] versus electrostatic and structural imprinting in this study) and the ability to tune the doping density in the target layer and to turn on/off the moiré potential by gating (both are not possible in Ref. [11]). Our study is also distinct from Ref. [21] and [39]. The device structure in the former is not able to probe the effects of moiré imprinting in the target layer; that in the latter has a different origin for the moiré potential, which is also not gate

tunable. Our results demonstrate the ability to control moiré lattices by electrostatic gating and open the door for dynamical control of moiré potentials in future studies.

Methods

Device fabrication. The heterostructures were fabricated by the layer-by-layer dry transfer technique [40]. Figure 1a shows the schematic cross section of the heterostructure. Extended Data Fig. 1 shows the optical images of device 1 and 2. We exfoliate the constituent layers from their bulk crystals and identify their thicknesses under an optical microscope; more accurate thickness determination was achieved using an atomic force microscope (AFM). To assemble the desired heterostructure, we first angle align the $MoSe_2$ and WS_2 monolayers to form the moiré layer using polarization- and angle-resolved second-harmonic generation spectroscopy [28, 29]; we then stack the constituent layers in the desired sequence following the procedures reported by earlier studies [21, 22]. The target layer $MoSe_2$ was not angle aligned with the moiré bilayer. The thickness of the hBN spacer (d_2) between the moiré and target layer is four and two layers in device 1 and 2, respectively, and that (d_1) between the WSe_2 exciton sensor and the target layer is 3-4 layers. The top and bottom gates are nearly symmetric in thickness with few-layer graphite gate electrodes and hBN gate dielectrics. The top and bottom gate hBN thicknesses are $d_t \approx 15.8$ nm and $d_b \approx 15.4$ nm for device 1 and $d_t \approx 10.1$ nm and $d_b \approx 10.2$ nm for device 2. In the limit of $d_t \approx d_b \gg d_1, d_2$, the total doping density is $n \approx \frac{\varepsilon_{hBN}\varepsilon_0}{2ed_t}(V_t + V_b)$; the applied electric field is $E \approx \frac{1}{2}(\frac{V_t}{d_t} - \frac{V_b}{d_b}) \approx \frac{1}{2d_t}(V_t - V_b)$. Here ε_0 and ε_{hBN} denote the vacuum permittivity and the hBN dielectric constant, respectively. We define a downward pointing electric field as a positive electric field.

Optical measurements. The devices were characterized by optical reflection spectroscopy. They were mounted in a Montana cryostation (Standard series) with base temperature about 5 K. We focused white light from a tungsten halogen lamp onto the devices with ~ 1 μm spot size using a microscope objective (Olympus LUCPlanFLN ×40, 0.6 NA). The total incident power was less than 1 nW. The reflected light from the devices was collected by the same objective and sent to a spectrometer equipped with a charge-coupled device (CCD) for spectrum analysis. To obtain the reflectance contrast spectrum R, we used the reflectance spectrum from the sample at a large hole or electron doping density as a background, at which all the exciton features become negligible, and then normalized the reflectance spectra at arbitrary gate voltages to this background.

Extraction of the exciton reflectance contrast amplitudes. To plot the phase diagram in Fig. 4 and Extended Data Fig. 4 and 6, we took the maximum reflectance contrast in the spectral range of 1.59-1.61eV for the fundamental moiré exciton MX_1, of 1.636-1.65 eV for the excited moiré exciton MX_2, of 1.618-1.628 eV for the charged exciton X^- in the target layer, and of 1.823-1.873 eV for the 2s exciton in the sensor. To enhance the contrast of the 2s exciton with respect to the background, we further took the first and second derivatives of the 2s reflectance contrast spectrum with respect to the photon energy ϵ ($\frac{dR}{d\epsilon}$ and $\frac{d^2R}{d\epsilon^2}$) and extracted the maximum value.

2s exciton sensing. Excitons in monolayer transition metal dichalcogenides (TMDs) support Rydberg-like bound states (e.g. 1s, 2s …) in the optical absorption spectrum [41]. Because of the atomic thickness of the material, the electrostatic field lines responsible for electron-hole binding reside largely outside the monolayer material. The exciton binding energy is therefore highly sensitive to the dielectric environment surrounding the material [30]. In particular, a metallic (or compressible) sample with large dielectric constant in close proximity to the TMD monolayer would effectively screen the electrostatic field lines for binding, resulting in a weaker excitonic binding compared to the case of an insulating (or incompressible) sample with small dielectric constant. A smaller exciton binding energy (i.e. a smaller energy difference between the 1s and 2s Rydberg states) and a weaker excitonic resonance or oscillator strength are thus expected for a metallic sample. This allows us to use the TMD monolayer as a sensor to probe the compressibility and the emergence of insulating states in the sample [15]. In our experiment, we monitored the 2s rather than the 1s Rydberg state for sensing because of the larger Bohr radius and therefore better sensitivity for the former.

Additional discussions on the electrostatics phase diagram. The top and bottom gates allow us to independently tune the total doping density and the vertical electric field in the device. The latter controls the charge carrier distribution between the moiré and the target layer at a fixed total doping density. In particular, a large downward (upward) electric field pushes all of the electrons to the target (moiré) layer. The higher the doping density, the higher the electric field is required to fully polarize all of the electrons to a particular layer; this explains the general upward and downward dispersion of the solid pink and black line, respectively, in Fig. 1b. Here the pink (black) line corresponds to the Fermi level locked to the conduction band minimum of the moiré (target) layer [21]. There are vertical jumps of the black line at integer filling factors; they correspond to the chemical potential jumps (or charge gaps) at the incompressible states of the moiré layer [21]. In order to sweep the Fermi level through the charge gap, we need to generate a Stark shift between the bands of the two layers (by an amount equal to the charge gap) at a constant filling; this results in an electric field jump. The jumps also create regions bound by the pink dashed lines in the phase diagram; these regions correspond to the Fermi level inside the charge gap of the moiré layer [21] (i.e. ν_m is fixed at an integer value). The electric field jumps are nearly absent for the pink line because of the negligible charge gaps in the target layer with a weak moiré imprinting effect.

Stability of the insulating states in the target layer other than $\nu_t = 1$. As a result of the weak moiré potential from electrostatic imprinting (Extended Data Fig. 7), we observe a correlated insulating state only at $\nu_t = 1$ in the target layer. Both the incompressible states at $\nu_t = 2$ and at commensurate fractional ν_t are unstable. The insulating state at $\nu_t = 2$ requires trapping of two electrons per moiré unit cell. The moiré potential depth (about 4 meV and is comparable to the electron kinetic energy of the target layer at the moiré density) is, however, substantially weaker than the Coulomb repulsion between the two electrons (about 100 meV). The electrons are thus delocalized (or "ionized") and the state becomes compressible. For commensurate fractional ν_t, the formation of a generalized Wigner crystal state requires a small electron kinetic energy compared to the long-range Coulomb repulsion between the electrons [15]. A weak moiré

potential, however, favors higher electron kinetic energy and therefore destabilizes the incompressible states at fractional ν_t.

Estimate of disorder level broadening. The typical disorder density in TMD materials is about $n_d = 10^{11}$ cm^{-2} (Ref. [42]). We can estimate the disorder-induced energy level broadening by $\frac{\pi\hbar^2}{m^*} n_d \approx 0.5$meV, in which $m^* \approx 0.5 m_0$ is the typical effective mass in monolayer TMDs (m_0 is the free electron mass). The disorder level broadening is much smaller than the trapping depth (about 4 meV) of the imprinted potential.

References

1. Andrei, E.Y. et al. The marvels of moiré materials. *Nature Reviews Materials* **6**, 201-206 (2021).
2. Andrei, E.Y. & MacDonald, A.H. Graphene bilayers with a twist. *Nature Materials* **19**, 1265-1275 (2020).
3. Balents, L., Dean, C.R., Efetov, D.K. & Young, A.F. Superconductivity and strong correlations in moiré flat bands. *Nature Physics* **16**, 725-733 (2020).
4. Cao, Y. et al. Unconventional superconductivity in magic-angle graphene superlattices. *Nature* **556**, 43-50 (2018).
5. Kennes, D.M. et al. Moiré heterostructures as a condensed-matter quantum simulator. *Nature Physics* **17**, 155-163 (2021).
6. Mak, K.F. & Shan, J. Semiconductor moiré materials. *Nature Nanotechnology* **17**, 686-695 (2022).
7. Wu, F., Lovorn, T., Tutuc, E. & MacDonald, A.H. Hubbard Model Physics in Transition Metal Dichalcogenide Moire Bands. *Physical Review Letters* **121**, 026402 (2018).
8. Wu, F., Lovorn, T., Tutuc, E., Martin, I. & MacDonald, A.H. Topological Insulators in Twisted Transition Metal Dichalcogenide Homobilayers. *Physical Review Letters* **122**, 086402 (2019).
9. Bistritzer, R. & MacDonald, A.H. Moiré bands in twisted double-layer graphene. *Proceedings of the National Academy of Sciences* **108**, 12233-12237 (2011).
10. Li, H. et al. Imaging moiré flat bands in three-dimensional reconstructed WSe2/WS2 superlattices. *Nature Materials* **20**, 945-950 (2021).
11. Xu, Y. et al. Creation of moiré bands in a monolayer semiconductor by spatially periodic dielectric screening. *Nature Materials* **20**, 645-649 (2021).
12. Wang, F. et al. (Research Square, 2022).
13. Kim, K. et al. Spin-Conserving Resonant Tunneling in Twist-Controlled WSe2-hBN-WSe2 Heterostructures. *Nano Letters* **18**, 5967-5973 (2018).
14. Tang, Y. et al. Dielectric catastrophe at the Wigner-Mott transition in a moiré superlattice. *Nature Communications* **13**, 4271 (2022).
15. Xu, Y. et al. Correlated insulating states at fractional fillings of moiré superlattices. *Nature* **587**, 214-218 (2020).
16. Shi, Q. et al. Bilayer WSe2 as a natural platform for interlayer exciton condensates in the strong coupling limit. *Nature Nanotechnology* **17**, 577-582 (2022).

17. Xu, Y. et al. A tunable bilayer Hubbard model in twisted WSe2. *Nature Nanotechnology* **17**, 934-939 (2022).
18. Chen, D. et al. Excitonic insulator in a heterojunction moiré superlattice. *Nature Physics* **18**, 1171-1176 (2022).
19. Li, T. et al. Quantum anomalous Hall effect from intertwined moiré bands. *Nature* **600**, 641-646 (2021).
20. Zhao, W. et al. Gate-tunable heavy fermions in a moir\'e Kondo lattice. *arXiv preprint arXiv:2211.00263* (2022).
21. Gu, J. et al. Dipolar excitonic insulator in a moiré lattice. *Nature Physics* **18**, 395-400 (2022).
22. Zhang, Z. et al. Correlated interlayer exciton insulator in heterostructures of monolayer WSe2 and moiré WS2/WSe2. *Nature Physics* **18**, 1214-1220 (2022).
23. Huang, D., Choi, J., Shih, C.-K. & Li, X. Excitons in semiconductor moiré superlattices. *Nature Nanotechnology* **17**, 227-238 (2022).
24. Regan, E.C. et al. Emerging exciton physics in transition metal dichalcogenide heterobilayers. *Nature Reviews Materials* **7**, 778-795 (2022).
25. Wilson, N.P., Yao, W., Shan, J. & Xu, X. Excitons and emergent quantum phenomena in stacked 2D semiconductors. *Nature* **599**, 383-392 (2021).
26. Mak, K.F. & Shan, J. Photonics and optoelectronics of 2D semiconductor transition metal dichalcogenides. *Nature Photonics* **10**, 216-226 (2016).
27. Zeng, Y. et al. Exciton density waves in Coulomb-coupled dual moiré lattices. *Nature Materials*, 1-5 (2023).
28. Regan, E.C. et al. Mott and generalized Wigner crystal states in WSe2/WS2 moiré superlattices. *Nature* **579**, 359-363 (2020).
29. Tang, Y. et al. Simulation of Hubbard model physics in WSe2/WS2 moiré superlattices. *Nature* **579**, 353-358 (2020).
30. Raja, A. et al. Coulomb engineering of the bandgap and excitons in two-dimensional materials. *Nature Communications* **8**, 15251 (2017).
31. Ma, L. et al. Strongly correlated excitonic insulator in atomic double layers. *Nature* **598**, 585-589 (2021).
32. Li, H. et al. Imaging two-dimensional generalized Wigner crystals. *Nature* **597**, 650-654 (2021).
33. Shimazaki, Y. et al. Optical Signatures of Periodic Charge Distribution in a Mott-like Correlated Insulator State. *Physical Review X* **11**, 021027 (2021).
34. Li, T. et al. Charge-order-enhanced capacitance in semiconductor moiré superlattices. *Nature Nanotechnology* **16**, 1068-1072 (2021).
35. Liu, X. et al. Visualizing broken symmetry and topological defects in a quantum Hall ferromagnet. *Science* **375**, 321-326 (2022).
36. Jin, C. et al. Stripe phases in WSe2/WS2 moiré superlattices. *Nature Materials* **20**, 940-944 (2021).
37. Halbertal, D. et al. Multilayered Atomic Relaxation in van der Waals Heterostructures. *Physical Review X* **13**, 011026 (2023).
38. Zhang, Y., Yuan, N.F.Q. & Fu, L. Moir\'e quantum chemistry: Charge transfer in transition metal dichalcogenide superlattices. *Physical Review B* **102**, 201115 (2020).

39. Shimazaki, Y. et al. Strongly correlated electrons and hybrid excitons in a moiré heterostructure. *Nature* **580**, 472-477 (2020).
40. Wang, L. et al. One-Dimensional Electrical Contact to a Two-Dimensional Material. *Science* **342**, 614-617 (2013).
41. Wang, G. et al. Colloquium: Excitons in atomically thin transition metal dichalcogenides. *Reviews of Modern Physics* **90**, 021001 (2018).
42. Rhodes, D., Chae, S.H., Ribeiro-Palau, R. & Hone, J. Disorder in van der Waals heterostructures of 2D materials. *Nature Materials* **18**, 541-549 (2019).

Figures

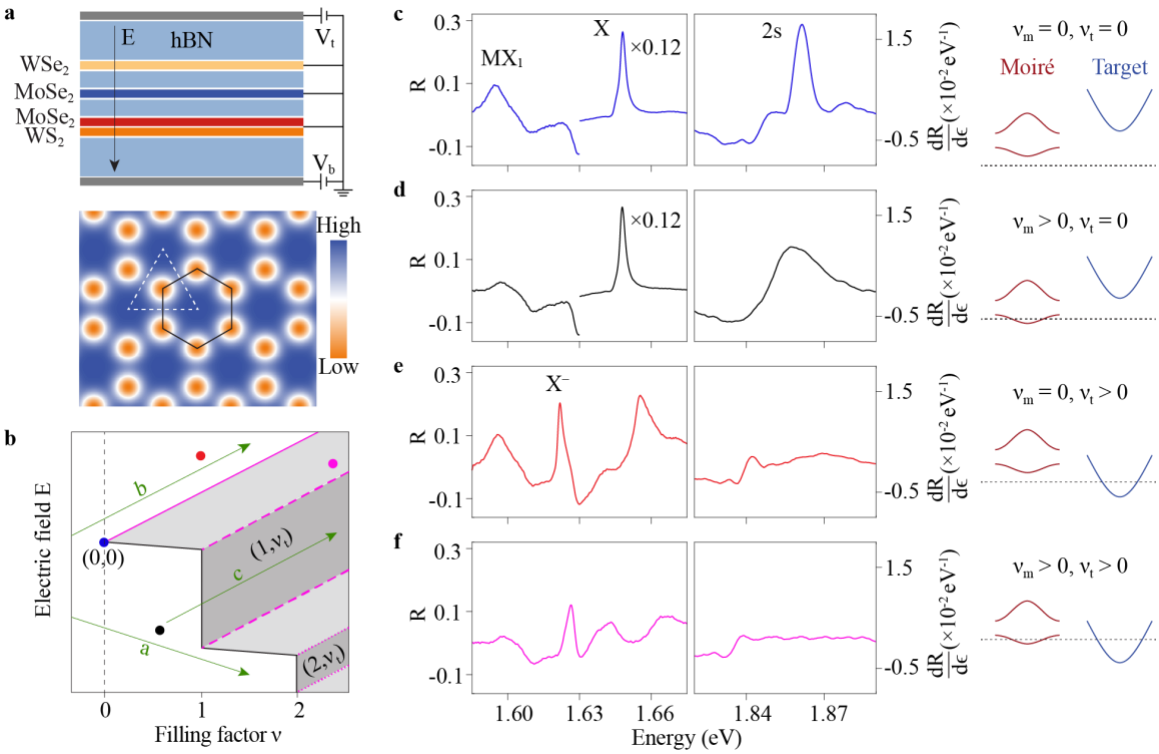

Figure 1 | Experimental setup. a, Top: device schematic. The target material ($MoSe_2$ monolayer) is separated from the moiré layer (angle-aligned $MoSe_2/WS_2$) by a 2-4-layer hBN spacer. The WSe_2 monolayer is an exciton sensor. The top and bottom gate voltages (V_t and V_b) control independently the perpendicular electric field E and the total doping density ν in the two $MoSe_2$ layers. Downward direction corresponds to $E > 0$. Bottom: schematic 2D electrostatic potential profile. A honeycomb moiré lattice (black line) can be imprinted onto the target material by a triangular electron lattice (white dashed line) in the moiré layer. **b**, Schematic electrostatics phase diagram with (ν_m, ν_t) denoting doping density in the moiré and target layers, respectively. Different lines label the region boundaries. The charge-sharing regions are shaded in grey. Gate voltages are swept along the three arrowed lines for **Fig. 2a-c**. **c-f**, Reflectance contrast spectrum (R) of device 1 at four points on the phase diagram in **b** with matched colors. MX_1, X, X^- and 2s denote, respectively, the fundamental moiré exciton, the neutral and charged excitons of the target layer, and the 2s exciton of the sensor layer (the first energy derivative of the 2s spectrum, $\frac{dR}{d\epsilon}$, is chosen to bring out more the feature). The X feature in **c** and **d** is scaled by a factor of 0.12. Right column shows the corresponding conduction band alignment. The bands for the moiré layer are the lower and upper Hubbard bands. The dotted lines label the Fermi level.

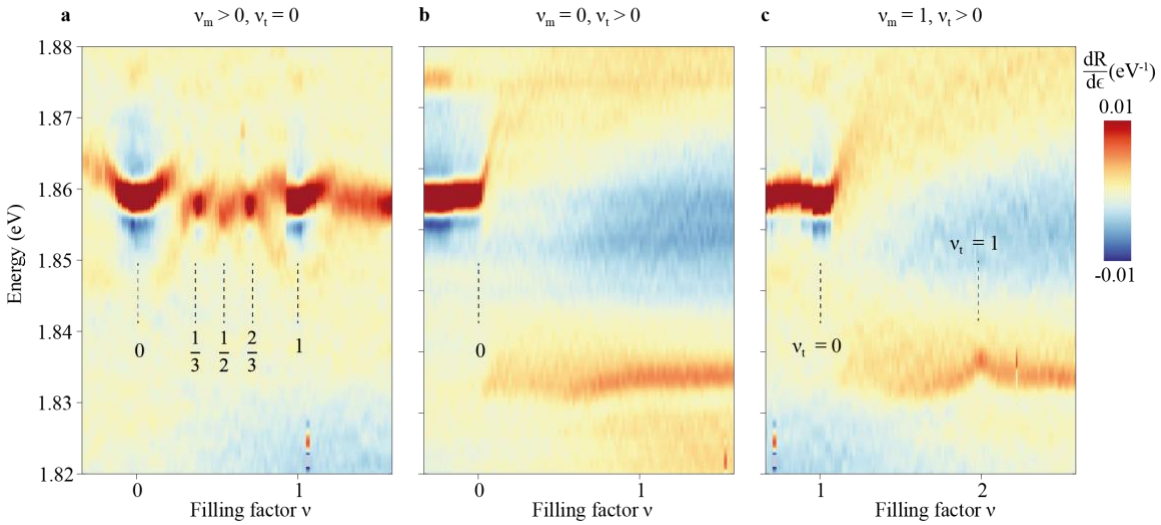

Figure 2 | Imprinted moiré potential in device 1 (4-layer hBN spacer). a-c, First energy derivative of the sensor 2s spectrum ($\frac{dR}{d\epsilon}$) as a function of the total filling factor. The gate voltages are scanned along the three arrowed lines in **Fig. 1b** with $\nu_m > 0$ and $\nu_t = 0$ (**a**), $\nu_m = 0$ and $\nu_t > 0$ (**b**) and $\nu_m = 1$ and $\nu_t > 0$ (**c**). Incompressible states are labeled by their filling factors.

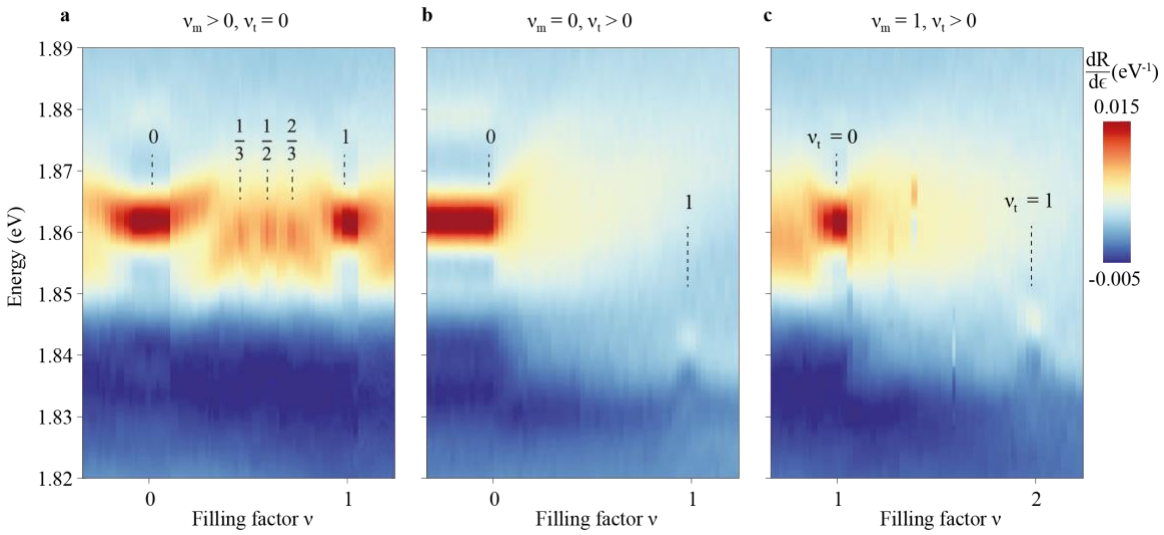

Figure 3 | Imprinted moiré potential in device 2 (2-layer hBN spacer). a-c, First energy derivative of the sensor 2s spectrum ($\frac{dR}{d\epsilon}$) as a function of the total filling factor. As in **Fig. 2**, the three cases correspond to $\nu_m > 0$ and $\nu_t = 0$ (**a**), $\nu_m = 0$ and $\nu_t > 0$ (**b**) and $\nu_m = 1$ and $\nu_t > 0$ (**c**). Incompressible states are labeled by their filling factors. The sudden jumps near the insulating states are originated from the nonlinear gating due to the unstable electrical contacts to the sample.

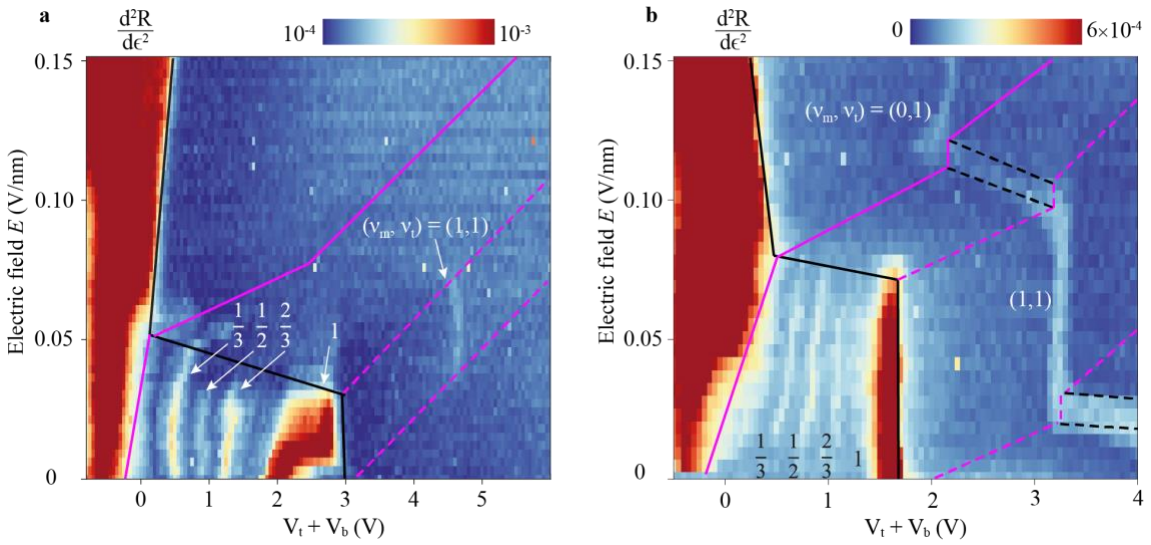

Figure 4 | Mechanisms for remote imprinting of moiré potentials. a,b, Second energy derivative of the 2s exciton reflectance contrast ($\frac{d^2R}{d\epsilon^2}$) as function of the gate voltage ($V_t + V_b$) and the electric field (E) for device 1 (**a**) and device 2 (**b**). The maximum amplitude of $\frac{d^2R}{d\epsilon^2}$ in the range of 1.823-1.873 eV is shown. The incompressible states are labeled by their filling factor (ν_m, ν_t). The phase boundaries (labeled by lines of the same color and style as in **Fig. 1b**) are determined by the reflectance contrast of the different exciton species (Extended Data Fig. 3-6). Dispersions of the phase boundaries and the incompressible states (especially at low doping densities) are caused by the nonlinear gating effect due to the high contact resistance. The $\nu_t = 1$ incompressible state is observed only at $\nu_m = 1$ in device 1; it is robust regardless of ν_m in device 2.

Extended Data Figures

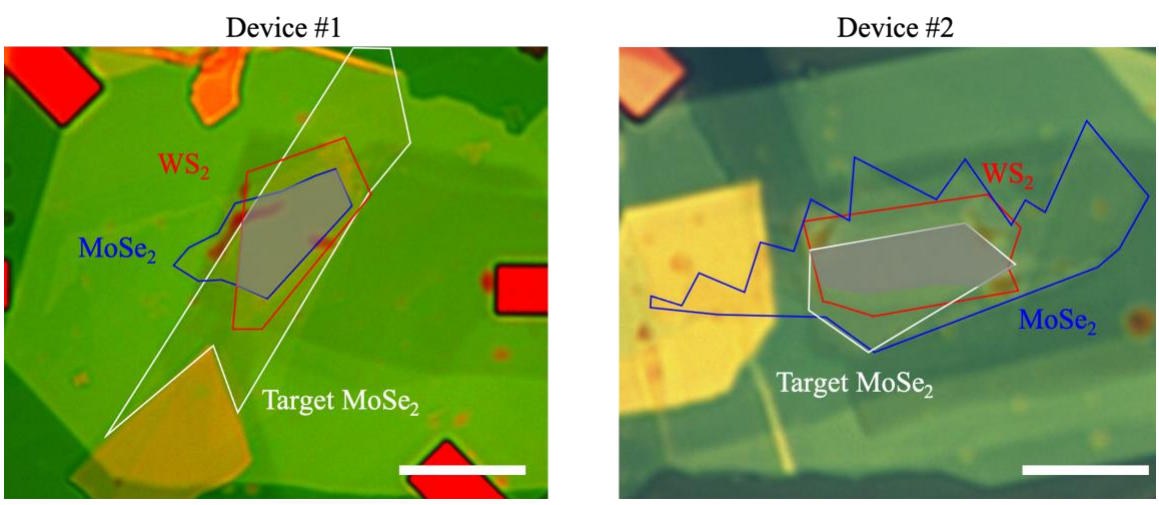

Extended Data Figure 1 | Optical image of device 1 and 2. The target $MoSe_2$ monolayer (white) and the moiré bilayer with monolayer $MoSe_2$ (blue) and WS_2 (red) are labeled and outlined. The effective area of the devices is shaded in grey. The scale bars are 10 μm.

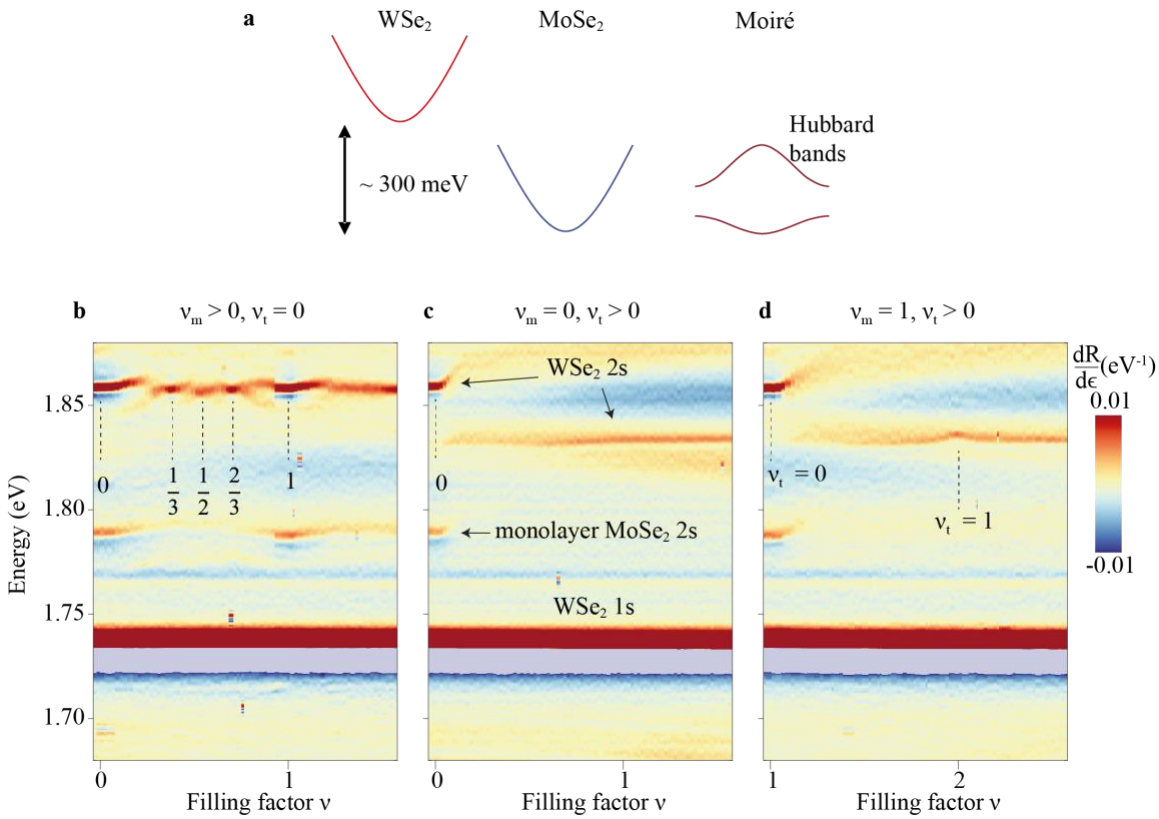

Extended Data Figure 2 | Charge neutrality of the sensor. **a**. Conduction band alignment for the TMD layers involved in the device structure under zero external electric field. **b-d**, First energy derivative of the sensor reflection contrast spectrum ($\frac{dR}{d\epsilon}$) as a function of the total filling factor. The gate voltages are scanned along the three arrowed lines in **Fig. 1b** with $\nu_m > 0$ and $\nu_t = 0$ (**b**), $\nu_m = 0$ and $\nu_t > 0$ (**c**) and $\nu_m = 1$ and $\nu_t > 0$ (**d**). Incompressible states are labeled by their filling factors. The 1s and 2s excitons of the WSe_2 sensor layer as well as the 2s exciton of the $MoSe_2$ target layer are labeled. The robust 1s exciton resonance of the WSe_2 layer, irrespective of the filling factor, demonstrates the charge neutrality of the sensor.

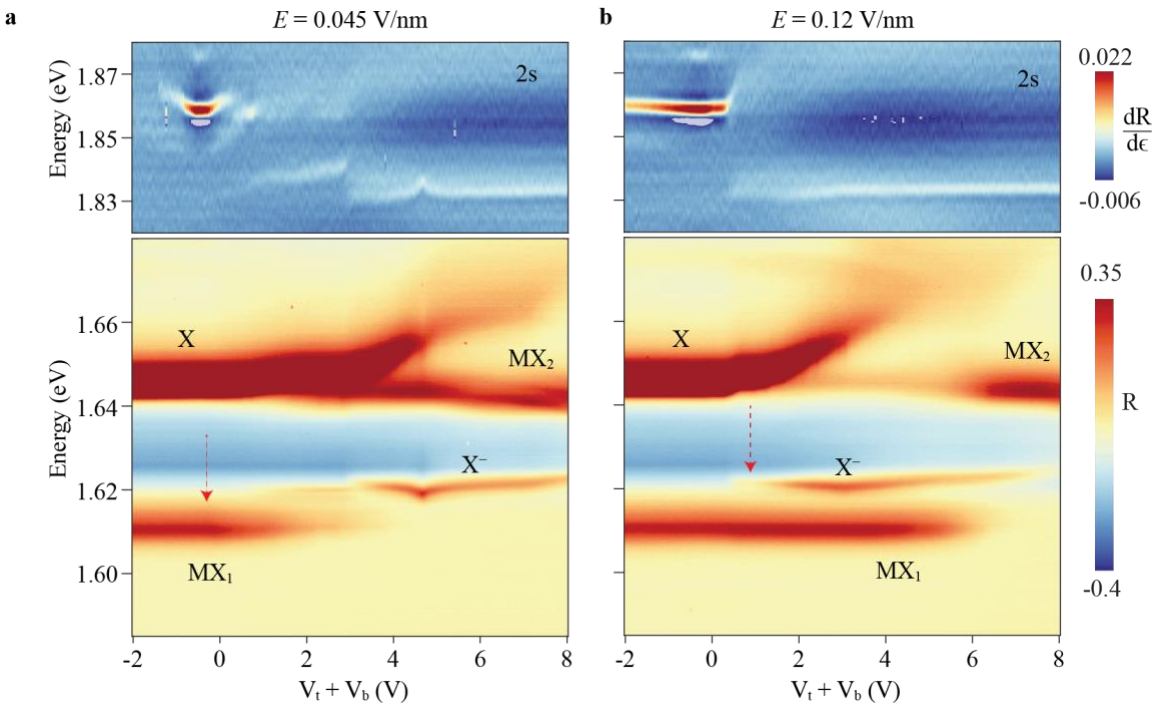

Extended Data Figure 3 | Gate dependent reflectance contrast spectrum (device 1). **a,b**, Gate voltage ($V_t + V_b$) dependent reflectance contrast spectrum at electric field 0.045 V/nm (**a**) and 0.12 V/nm (**b**). Five different exciton species can be identified: the fundamental moiré exciton MX_1, the excited moiré exciton MX_2, the neutral (X) and charged (X^-) excitons of the target layer, and the 2s exciton of the sensor layer. The red dashed arrows denote the onset of electron doping in the device. The moiré (target) layer is first doped at low (high) electric field.

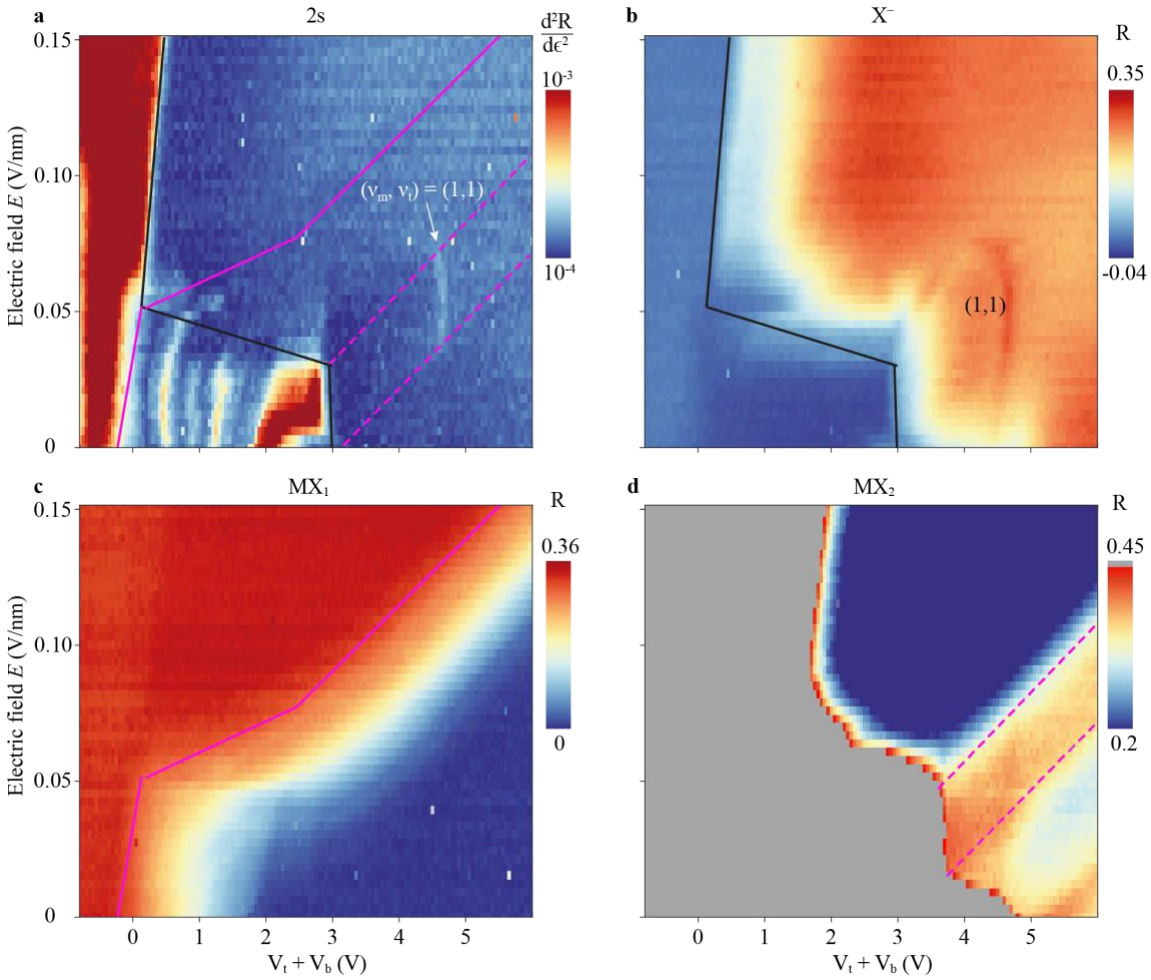

Extended Data Figure 4 | Electrostatics phase diagram (device 1). a-d, Electric-field (E) and gate ($V_t + V_b$) dependences of the spectral feature corresponding to the sensor 2s exciton (**a**), charged exciton X^- of the target layer (**b**), moiré exciton MX_1 (**c**) and MX_2 (**d**). The analysis of the reflectance contrast spectra is described in Methods. The X^- reflectance (**b**) determines the boundary between the doped (high) and neutral (low) target layer (black solid line). The MX_1 reflectance (**c**) determines the boundary between the doped (low) and neutral (high) moiré layer (pink solid line). The MX_2 reflectance (**d**) determines the boundaries of the $(\nu_m, \nu_t) = (1, \nu_t)$ region with enhanced contrast (pink dashed lines). These boundaries are included in **a**.

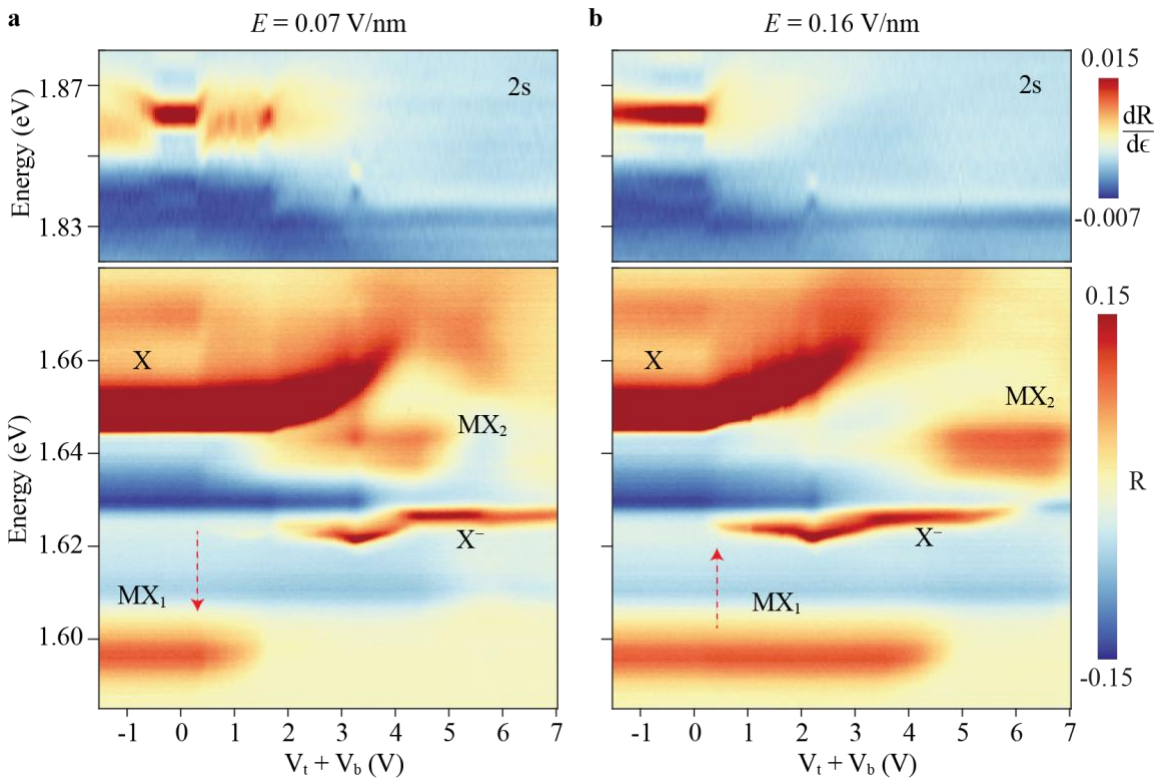

Extended Data Figure 5 | Gate dependent reflectance contrast spectrum (device 2). **a,b**, Gate voltage ($V_t + V_b$) dependent reflectance contrast spectrum at electric field 0.07 V/nm (**a**) and 0.16 V/nm (**b**). Similar to Extended Data Fig. 3, five different exciton species can be identified. The red dashed arrows denote the onset of electron doping in the device.

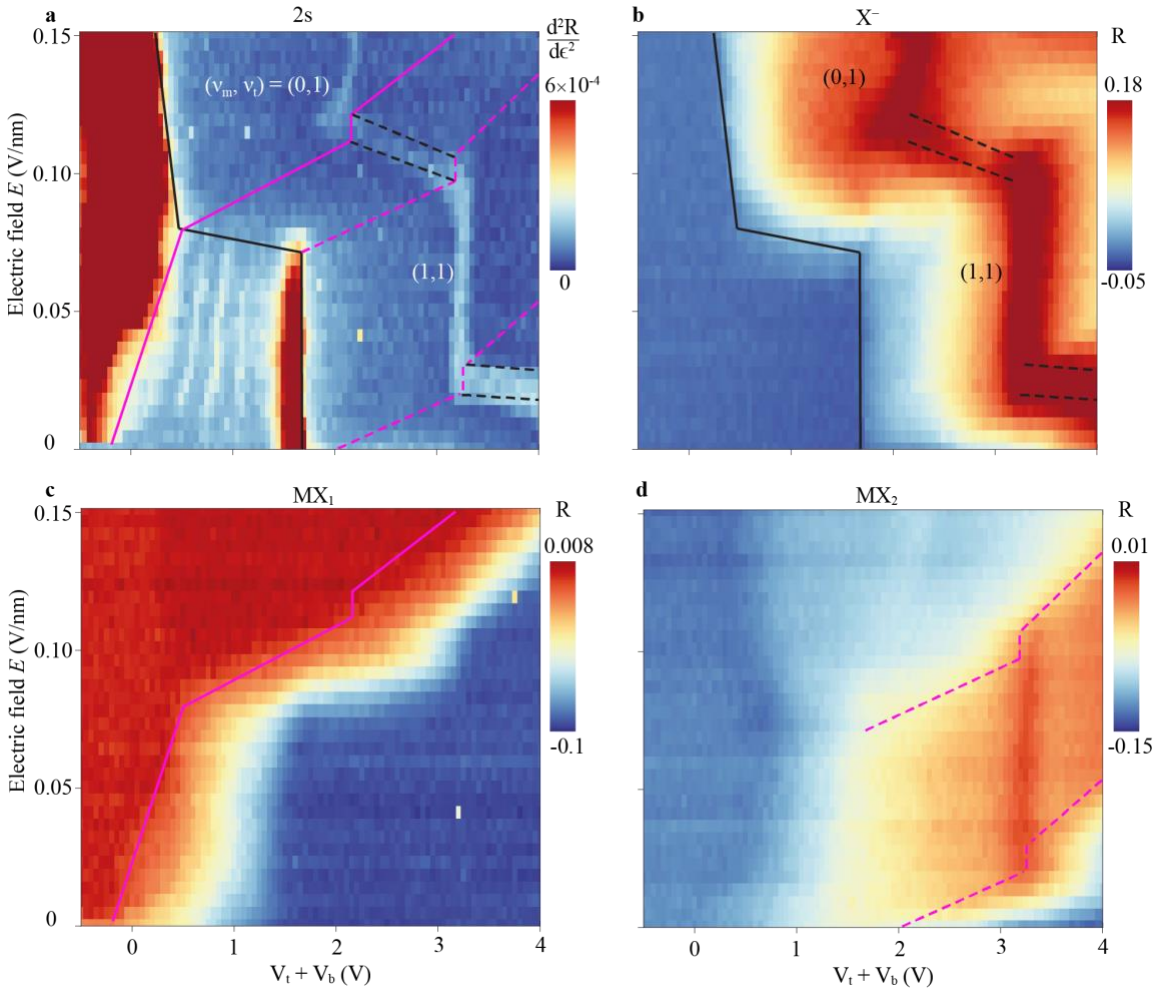

Extended Data Figure 6 | Electrostatics phase diagram (device 2). a-d, Electric-field (E) and gate ($V_t + V_b$) dependences of the spectral feature corresponding to the sensor 2s exciton (**a**), charged exciton X^- of the target layer (**b**), moiré exciton MX_1 (**c**) and MX_2 (**d**). The analysis of the reflectance contrast spectra is described in Methods. The X^- reflectance (**b**) determines the boundary between the doped (high) and neutral (low) target layer (black solid line). It also determines the boundaries (black dashed lines) of the $(\nu_m, \nu_t) = (\nu_m, 1)$ region. The MX_1 reflectance (**c**) determines the boundary between the doped (low) and neutral (high) moiré layer (pink solid line). The MX_2 reflectance (**d**) determines the boundaries of the $(\nu_m, \nu_t) = (1, \nu_t)$ region with enhanced contrast (pink dashed lines). These boundaries are included in **a**.

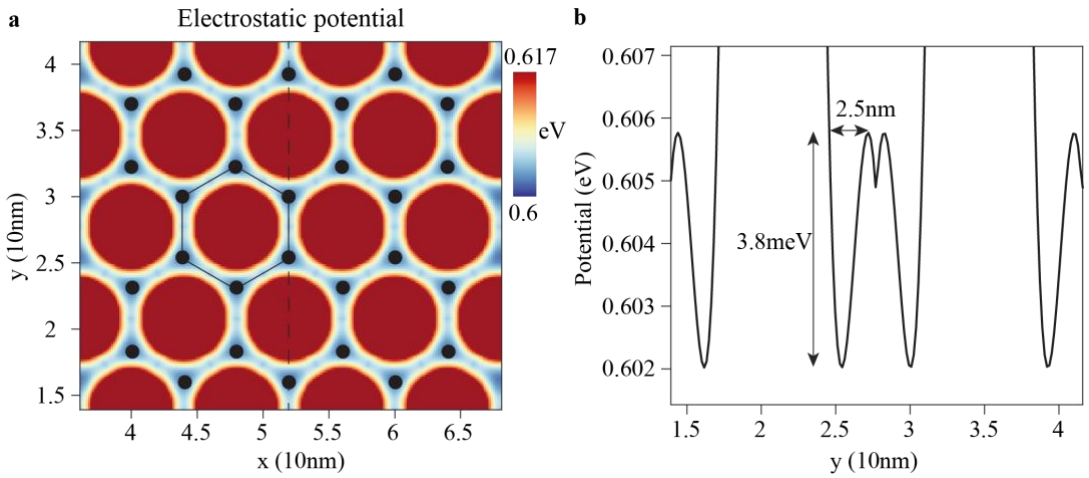

Extended Data Figure 7 | Electrostatic potential imprinted from a triangular electron lattice. a, Calculated electrostatic potential profile in a plane that is 1 nm above a triangular electron lattice. To mimic the real moiré lattice, we set the period to 8 nm in the calculation and used the dielectric constant of hBN. The triangular electron lattice imprints a honeycomb potential profile (black line denotes the unit cell and dots denote the sublattice sites). **b,** Electrostatic potential along the dashed line in **a**. It shows a trapping potential depth of about 4 meV.

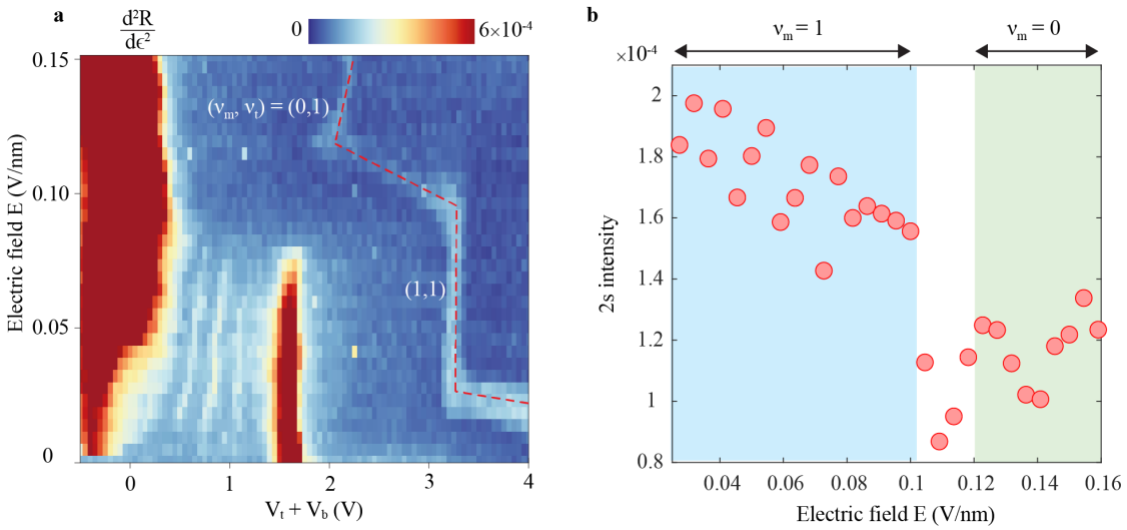

Extended Data Figure 8 | Electric field dependence of the 2s intensity in device 2. **a**, Second energy derivative of the 2s exciton reflectance contrast ($\frac{d^2R}{d\epsilon^2}$) as function of the gate voltage ($V_t + V_b$) and the electric field (E) for device 2. **b**, Extracted 2s peak intensity as a function of the electric field along the red dashed line in **a**. The blue and green regions correspond to $\nu_m = 1$ and $\nu_m = 0$, respectively. The enhanced 2s intensity in the blue region suggests a more robust correlated insulating state at $\nu_t = 1$ due to the electrostatic imprinting effect.

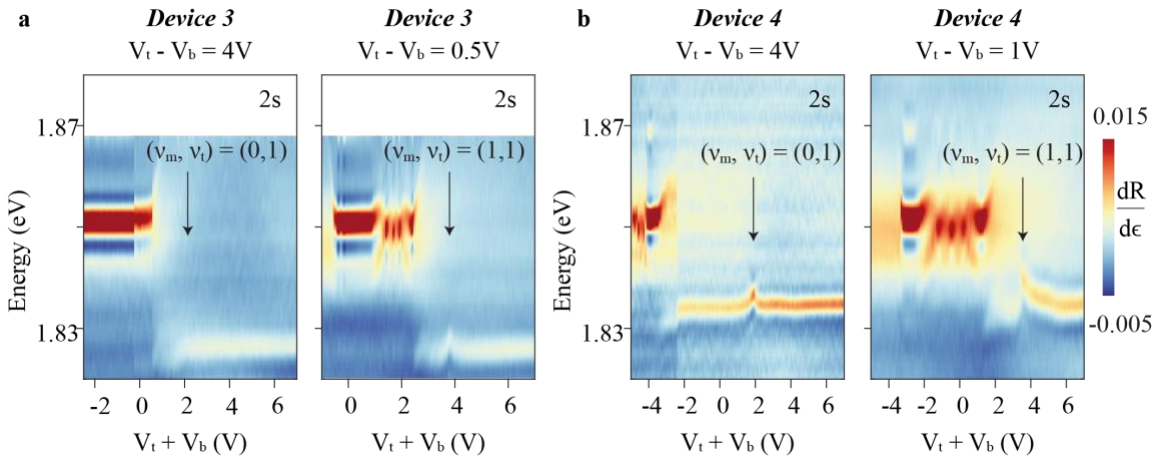

Extended Data Figure 9 | Results from additional devices. a,b, First energy derivative of the sensor 2s spectrum ($\frac{dR}{d\epsilon}$) as a function of the gate voltage ($V_t + V_b$) for device 3 with a 4-layer hBN spacer (**a**) and device 4 with a 2-layer hBN spacer (**b**). The gate voltage ($V_t + V_b$) controls the total filling factor under a constant electric field (controlled by $V_t - V_b$). We label the incompressible states $(\nu_m, \nu_t) = (0,1)$ and $(1,1)$ on the left and right panels, respectively.